JOURNAL OF GEOPHYSICAL RESEARCH, VOL. 114, B12404, doi:10.1029/2008JB006273, 2009

Shear-induced dilatancy of fluid-saturated faults: Experiment and theory

Jon Samuelson,[1] Derek Elsworth,[1] and Chris Marone[1]

Received 23 December 2008; revised 18 September 2009; accepted 29 October 2009; published 18 December 2009.

[1] Pore fluid pressure plays an important role in the frictional strength and stability of tectonic faults. We report on laboratory measurements of porosity changes associated with transient increases in shear velocity during frictional sliding within simulated fine-grained quartz fault gouge (d_{50} = 127 μm). Experiments were conducted in a novel true triaxial pressure vessel using the double-direct shear geometry. Shearing velocity step tests were used to measure a dilatancy coefficient ($\varepsilon = \Delta\phi/\Delta\ln(v)$, where ϕ is porosity and v is shear velocity) under a range of conditions: background shearing rate of 1 μm/s with steps to 3, 10, 30, and 100 μm/s at effective normal stresses from 0.8 to 20 MPa. We find that the dilatancy coefficient ranges from 4.7×10^{-5} to 3.0×10^{-4} and that it does not vary with effective normal stress. We use our measurements to model transient pore fluid depressurization in response to dilation resulting from step changes in shearing velocity. Dilatant hardening requires undrained response with the transition from drained to undrained loading indexed by the ratio of the rate of porosity change to the rate of drained fluid loss. Undrained loading is favored for high slip rates on low-permeability thick faults with low critical slip distances. Although experimental conditions indicate negligible depressurization due to relatively high system permeability, model results indicate that under feasible, but end-member conditions, shear-induced dilation of fault zones could reduce pore pressures or, correspondingly, increase effective normal stresses, by several tens of megapascals. Our results show that transient increases in shearing rate cause fault zone dilation. Such dilation would tend to arrest nucleation of unstable slip. Pore fluid depressurization would exacerbate this effect and could be a significant factor in generation of slow earthquakes, nonvolcanic tremors, and related phenomena.

Citation: Samuelson, J., D. Elsworth, and C. Marone (2009), Shear-induced dilatancy of fluid-saturated faults: Experiment and theory, *J. Geophys. Res.*, *114*, B12404, doi:10.1029/2008JB006273.

1. Introduction

[2] Pore fluids play an important role in faulting via their effect on frictional strength and rock-fluid interactions. Of particular interest in recent studies is the interplay of fault zone dilation and compaction and the role that thermal pressurization may play in the nucleation of earthquake slip [*Rice and Rudnicki*, 1979; *Rudnicki and Chen*, 1988; *Rudnicki and Hsu*, 1988; *Marone et al.*, 1990; *Lockner and Byerlee*, 1994; *Segall and Rice*, 1995; *Sleep*, 1995; *Moore and Iverson*, 2002; *Rubin and Ampuero*, 2005; *Hillers and Miller*, 2006; *Rice*, 2006; *Rudnicki and Rice*, 2006; *Segall and Rice*, 2006; *Bizzarri and Cocco*, 2006a, 2006b; *Hillers and Miller*, 2007; *Ampuero and Rubin*, 2008; *Mitchell and Faulkner*, 2008; *Perfettini and Ampuero*, 2008; *Rubin*, 2008; *Savage and Langbein*, 2008; *Song and Renner*, 2008]. These processes can change the effective normal stresses on a fault zone [*Hubbert and Rubey*, 1959] while tectonic stresses remain unchanged. The relationship between tectonic and effective normal stresses is defined as

$$\sigma' = \sigma_N - P_P, \tag{1}$$

where σ' is the effective normal stress, σ_N is the tectonic normal stress, and P_P is the pore fluid pressure. Reductions in P_P increase effective normal stress while increases in P_P reduce effective normal stress. Considering a simple Coulomb model for frictional strength

$$\tau = C + \mu\sigma', \tag{2}$$

where τ is shear strength, C is cohesion, and μ is the coefficient of internal friction, it is clear that the shear failure strength depends inversely on P_P.

[3] Pore fluids are thus thought to play an important role in stick-slip instability and earthquake rupture [e.g., *Bridgman*, 1936; *Brace and Byerlee*, 1966; *Scholz*, 2002]. We attempt here to quantify the effects of transients in effective normal

[1]Rock and Sediment Mechanics Laboratory, Center for Geomechanics, Geofluids, and Geohazards, and Energy Institute, Pennsylvania State University, University Park, Pennsylvania, USA.

0148-0227/09/2008JB006273$09.00

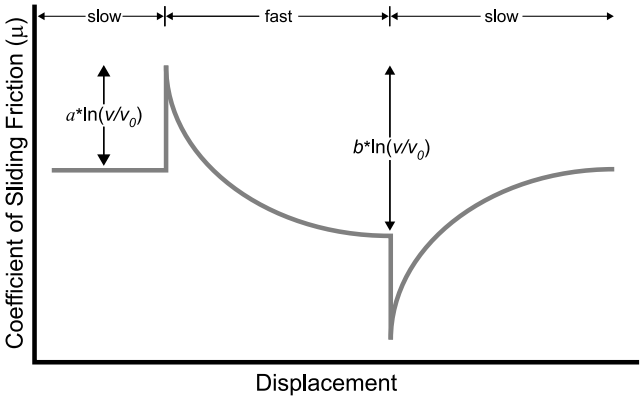

Figure 1. Idealized frictional response. For a step increase in loading velocity, friction increases by a*ln(v/v_0) and then decays over a characteristic sliding distance (D_C) by an amount b*ln(v/v_0) to a new steady state value. (a-b) > 0 implies a velocity strengthening material. (a-b) < 0 (as in the schematic) is a velocity weakening material. Note that schematic shows only frictional behavior, without elastic interaction.

stress in the context of rate- and state-dependent friction laws [*Dieterich*, 1979, 1981; *Ruina*, 1983]

$$\left.\begin{aligned} \mu &= \mu_0 + a\ln\left(\frac{v}{v_0}\right) + b\ln\left(\frac{v_0\theta}{D_C}\right) \\ \frac{d\theta}{dt} &= 1 - \frac{v\theta}{D_C} \quad \text{(Dieterich Evolution)} \\ \frac{d\theta}{dt} &= \frac{-v\theta}{D_C}\ln\left(\frac{v\theta}{D_C}\right) \quad \text{(Ruina Evolution)} \end{aligned}\right\}, \tag{3}$$

which describe the evolution of frictional strength as a function of sliding velocity, slip history (state), and normal stress. In equation (3), μ is the coefficient of friction, μ_o is a reference friction value defined at a reference sliding velocity v_0, v is sliding velocity, D_C is a critical slip distance (associated with changes in porosity and/or renewal of asperity contact junctions) and θ is a state variable, which is proportional to the average lifespan of asperity contacts and evolves with time and slip according to one of the evolution laws [*Dieterich*, 1978, 1979, 1981; *Ruina*, 1983]. The parameters a and b are scaling factors that determine whether friction is velocity weakening (a-b < 0) or velocity strengthening (a-b > 0) and are often measured using velocity step tests as shown schematically in Figure 1. In a velocity step test, a gouge layer is sheared until friction has reached a steady state and then the driving velocity is increased (or decreased) instantaneously (Figure 1). This increase in sliding velocity elicits an increase in the frictional resistance by an amount controlled by the so-called "direct effect," a, and the size of the velocity step. Friction then decays over a critical slip distance, D_C, to a new background value determined by the size of the velocity step and the "evolution effect," b.

[4] The rate- and state-dependent friction law can be written in terms of effective normal stresses as

$$\tau = (\sigma_N - P_P - \Delta P_P)\left[\mu_0 + a\ln\left(\frac{v}{v_0}\right) + b\ln\left(\frac{v_0\theta}{D_C}\right)\right], \tag{4}$$

where ΔP_P is a transient fluctuation in pore fluid pressure. For fault zone dilation and decompression of pore fluid, ΔP_P is negative and would act to increase shear strength via the increase in effective normal stress.

[5] A necessary condition for dilatant hardening is that the rate of fluid decompression exceeds the rate of pore fluid influx, i.e., pore space is created faster than it is pressurized with pore fluid. This phenomenon has been invoked as a possible mechanism of seismic quiescence [e.g., *Scholz*, 1988] as it would have the effect of inhibiting unstable slip along a fault by allowing the slip surface to frictionally strengthen in response to shear-induced dilation.

[6] Changes in porosity, $\Delta\phi$, associated with changes in sliding velocity have been shown to evolve over approximately the same slip distance, D_C, as frictional contacts in the rate and state friction law [*Marone et al.*, 1990]. Thus porosity may evolve as

$$\Delta\phi = -\varepsilon\ln\left(\frac{v_0\theta}{D_C}\right), \tag{5}$$

where ε is a scaling coefficient for the magnitude of dilation in response to a velocity step of any given size [*Segall and Rice*, 1995]. Several recent works have shown that fault zone dilation coupled with permeability, hydraulic properties of the fault zone, and shear heating are expected to have a significant influence on earthquake nucleation and dynamic weakening [*Rice*, 2006; *Rudnicki and Rice*, 2006; *Segall and Rice*, 2006; *Bizzarri and Cocco*, 2006a, 2006b; *Ampuero and Rubin*, 2008]. While much work has been done relating to dilatancy in rocks and granular materials [e.g., *Teufel*, 1981; *Bolton*, 1986; *Morrow and Byerlee*, 1989; *Marone et al.*, 1990], few laboratory observations of the dilatancy parameter are available.

[7] The purpose of this paper is to report measurements of this dilatancy coefficient, ε, for granular fault gouge and explore its variability and effect on pore pressure for a range of conditions. We focus in particular on fluid-saturated faults of finite layer perpendicular permeability and consider the role of transients in slip rate and/or stress. Much like sudden increases in fluid pressure might initiate slip on a fault surface, sudden decreases in fluid pressure associated with dilational decompression may play a role in inhibiting slip. We show that such decompression of pore fluids can be both sudden and significant.

2. Experimental Method

2.1. Experimental Technique

[8] Our experiments were conducted in a newly developed true triaxial pressure vessel, that extends the capabilities of the biaxial apparatus commonly used for friction measurements in our laboratory [e.g., *Mair and Marone*, 1999; *Karner and Marone*, 2001; *Frye and Marone*, 2002a; *Anthony and Marone*, 2005; *Ikari et al.*, 2007; *Savage and Marone*, 2007; *Johnson et al.*, 2008; *Niemeijer et al.*, 2008; *Rathbun et al.*, 2008; *Samuelson et al.*, 2008]. A more thorough description of the true triaxial apparatus is given in Appendix A, but we will focus here on the specific conditions used for these experiments.

[9] As with a conventional double-direct shear friction experiment, normal stress is applied to the simulated gouge

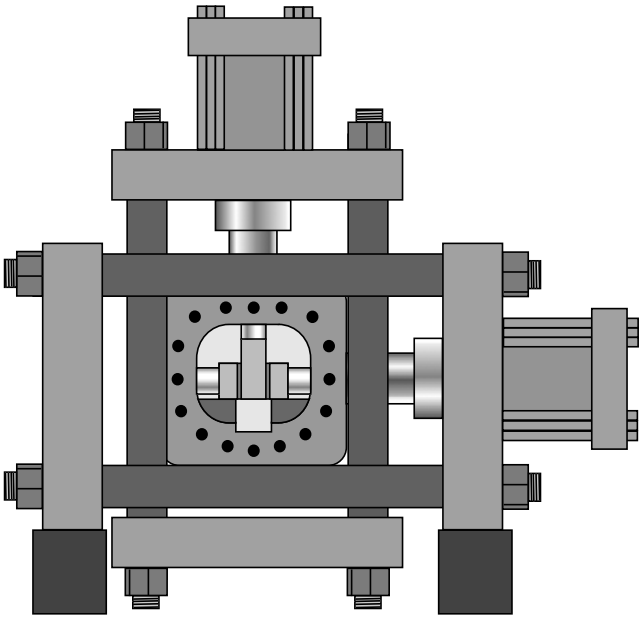

Figure 2. Sketch of the biaxial deformation apparatus including triaxial pressure vessel. For the double-direct shear configuration, three steel blocks sandwich two granular layers. The horizontal ram applies normal load to the layers, while the vertical ram drives the center block down to create shear load. The pressure vessel rests inside the biaxial apparatus, and loads are applied via pistons that enter through dynamic seals.

zone via a horizontally oriented hydraulic ram (Figure 2). Normal stress on the layers (5.7 cm × 5.4 cm nominal contact area) is maintained constant in load-feedback servo control (Figure 3). Shear stress is then applied by driving the vertically oriented hydraulic ram down, pushing the center forcing block through the granular layers in either load or displacement feedback mode. Both normal and shear loads were measured by load cells at a load point external to the pressure vessel with a precision of 0.1 kN. Displacement of the horizontal and vertical hydraulic rams were measured exterior to the pressure vessel using displacement transducers with 0.1 μm precision.

[10] Experiments were run under drained-saturated conditions using a constant pore pressure boundary condition. De-ionized water pore fluid was evenly distributed over the gouge layer using internal plumbing in the forcing blocks, and porous metal frits (Figure 3). Fluid pressures were monitored remote from the sample using pressure transducers with 0.007 MPa resolution. Load and displacement were measured external to the pressure vessel and recorded continuously at 10 kHz and sampled at rates from 1 to 10 Hz. Normal and shear stresses were resolved from the measured applied loads by dividing by the contact area of the forcing block in the case of normal stress, and twice the contact area in the case of shear stress [e.g., *Mair and Marone*, 1999; *Karner and Marone*, 2001; *Frye and Marone*, 2002a; *Frye and Marone*, 2002b; *Mair et al.*, 2002; *Anthony and Marone*, 2005; *Samuelson et al.*, 2008].

[11] Gouge layers were composed of F110, a high-purity (>99% quartz), fine-grained sand purchased from the U.S. Silica company; 95% of the grains are in the range 53–212 μm and the mean grain size is 127 μm. We independently determined the permeability of F110 subject to loads equal to those used in our study to be $\sim 10^{-13}$ m^2, by constant head permeability test in a uniaxial load frame [e.g., *Saffer and McKiernan*, 2005]. Gouge layers were constructed using a specially designed leveling jig to an initial thickness of 4 mm. Layer thickness was measured

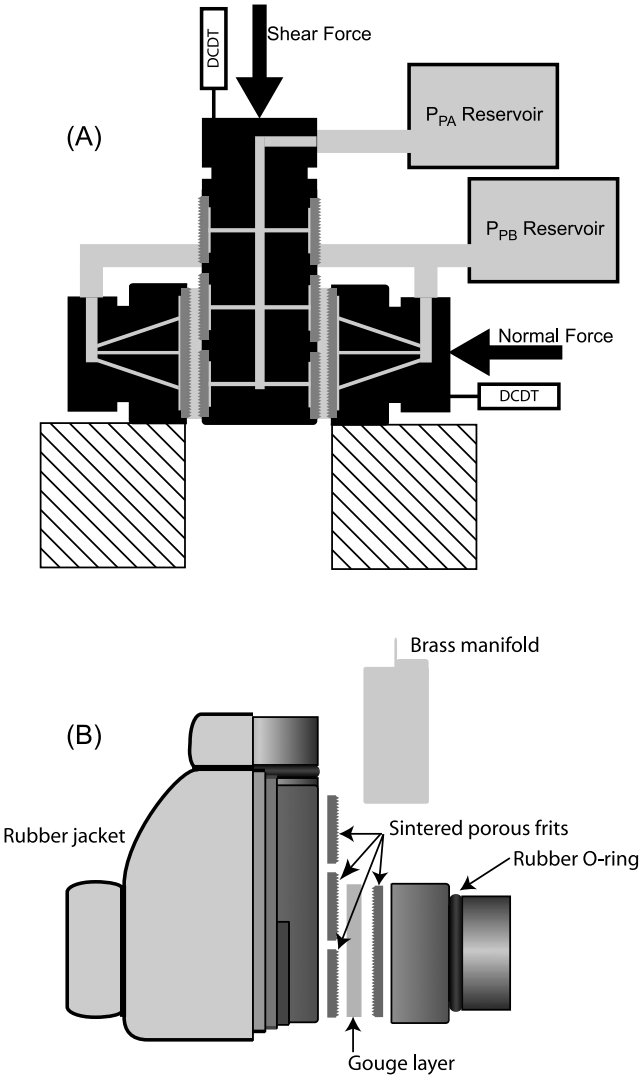

Figure 3. (a) Schematic of the forcing blocks and plumbing arrangement for pore fluid access. Gray ridged pieces at edges of forcing blocks (black) are sintered stainless steel fluid distribution frits. Pressure or flow rate boundary conditions can be applied on either side of the layer. (b) Fluid isolation system used in these experiments. From innermost to outermost the jacketing is a 3.2 mm thick latex rubber sheet, followed by 2 0.9 mm thick rubber sleeves, and finally two dip molded rubber jackets, sealed against the forcing blocks via an O-ring and steel wire. Also shown is a brass manifold that is placed under the rubber jacketing and over the forcing blocks around the gouge layer to prevent P_C from pressing the jacketing into the layer. As shown here, the thickness of the gouge layer (H) is as measured horizontally, and likewise ΔH is measured as changes in this horizontal thickness.

Table 1. Experiment Details[a]

Experiment	σ' (MPa)	Steady State Layer Thickness (μm)	Average (a-b)
p1459	30,20	3924.3	n/a, −6.7E-4
p1460	30,20	3906.6	n/a, −9.2E-4
p1449	15,10	3472.5	−4.9E-4, −8.6E-4
p1272	15	3942.9	−1.4E-3
p1450	6,2	3986.0	−3.1E-4, n/a
p1373	6,2	3820.1	n/a, n/a
p1374	0.8	3978.7	+

[a]Effective normal stresses include the order (high then low) in an experiment. The steady state layer thickness was used to normalize dilation values to obtain $\Delta\phi$. Average values of the friction rate parameter (a-b) are reported where data were available. Those data unavailable are represented by n/a, except p1374 which, though noisy, was clearly positive.

under applied normal load using calipers, prior to application of confining pressure while the pressure vessel door was open.

[12] In the case of these experiments the forcing blocks are jacketed using a latex rubber assembly (Figure 3b) in order to isolate confining pressure (P_C) from pore fluid pressure (P_P). The jacketing consisted of two dip molded latex rubber jackets approximately 1.5 mm thick manufactured by Piercan USA Inc. in San Marcos, California (Figure 3b). The jacketing procedure involved, first, a 3.2 mm thick latex rubber sheet around the bottom of the sample blocks, which prevented the jackets from being cut when the side forcing blocks were pressed against the support blocks beneath them (Figure 3a). This sheet was then wrapped with two 2.375″ diameter latex rubber sleeves 0.9 mm thick, which minimized jacket perforation from sample void space and the porous metal frits, each of which may come into contact with the jacket during shearing and offset. A final layer of protection, before the latex jackets are stretched over the sample assembly, was a thin brass cowling that rested on top of the side blocks, butting up against the center block and covering the top and sides of the layer edges to further prevent the jacket from being pushed into the layer by application of confining pressure. This successful jacketing and sealing system was developed through an extensive set of tests. From subsequent suites of experiments we know that our sealing success rate is nearly 90% and that the jackets have very little influence on the overall measured strength of the sample.

2.2. Experimental Procedure

[13] Experiments were conducted at effective normal stresses between 0.8 and 30 MPa. Individual experiments started with a high effective normal stress segment and then continued at a lower effective normal stress (30–20, 15–10, and 6–2 MPa), except in the case of the 0.8 MPa experiment, which was conducted using a single effective normal stress (Table 1). Data collected at 30 MPa were unusable, thus 20 MPa is the highest effective stress for which data are presented here. Effective normal stress (σ') was determined by the applied normal stress (σ_N), a fraction of the confining pressure (P_C) equal to the ratio of the piston contact area (44 mm diameter) to the layer area, and the measured pore pressure (P_P):

$$\sigma' = \sigma_N + 0.506P_C - P_P. \quad (6)$$

Confining pressure was set to 4.5, 2.5, and 1.5 MPa respectively in the 30–20, 15–10, 6–2 MPa experiments, while P_P was set at 4.0, 2.0, and 1.0 MPa. The 0.8 MPa experiment used $P_C = 0.5$ MPa and $P_P = 0.4$ MPa. Only the applied normal stress (σ_N) was varied to change the effective normal stress.

[14] Each experiment consisted of an initial shear loading phase at 10 μm/s both to compress the rubber and to reach steady state frictional sliding (Figure 4). After the initial run-in portion of the experiment the background loading rate was reduced to 1 μm/s and we conducted a series of velocity stepping experiments wherein the sliding velocity was stepped from 1 to 3 and back to 1 μm/s followed by steps to 10, 30, and 100 μm/s (Figure 4).

[15] Jacket stretching and rubber compression are removed via calibrations conducted by loading a sample with a solid block beneath the center block. In this configuration, layer shear cannot occur and we measure only rubber compression and the loading stiffness of the experimental sample. We have removed these effects from the data reported here. This correction results in the removal of several millimeters of displacement due to rubber compression, leaving only shear displacement at the boundaries of the gouge layer.

3. Experimental Observations

[16] Rate and state friction laws predict that a step increase in loading velocity should produce an instantaneous increase in the frictional strength that decays over a critical slip

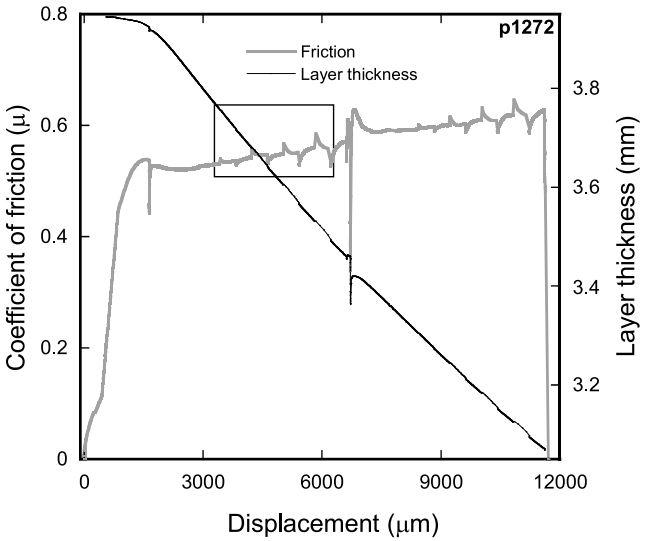

Figure 4. Representative curve showing frictional strength and layer thickness versus shear displacement. Friction has been corrected for apparatus stiffness, piston-seal friction, and jacket stretch. Experiments typically began with a high effective normal stress segment followed by a lower stress segment (Table 1). Vertical line between 6000 and 7000 μm represents a change from σ' of 15 to 10 MPa. An initial run-in at 10 μm/s was used to approach steady state friction (~1500 μm). After this, velocity step tests (boxed region) were conducted at each effective normal stress. Layers thin with displacement due to direct shear geometry. Close inspection of the layer thickness shows dilation concurrent with the frictional response to velocity step tests.

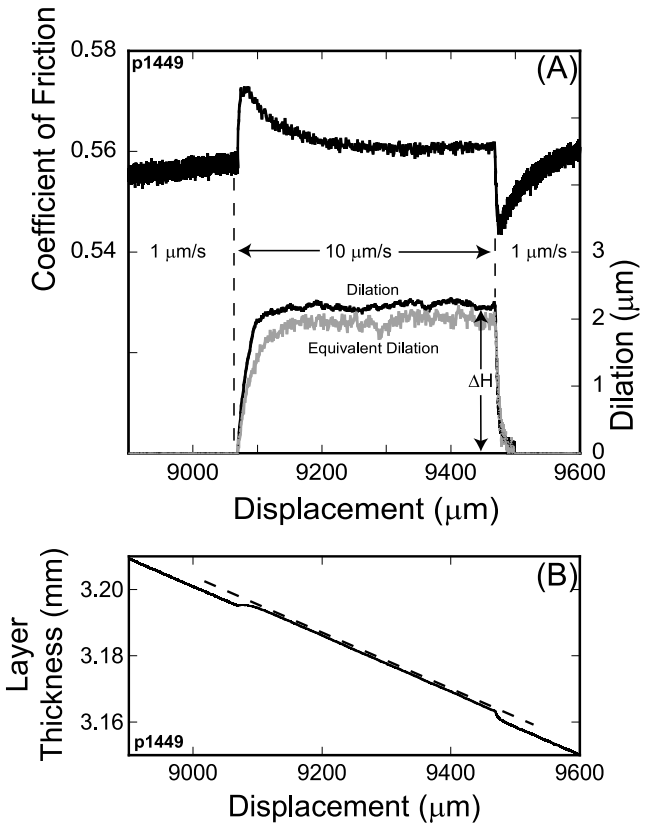

Figure 5. (a) Enlargement of velocity step test (Figure 4) showing frictional response (top curve) and accompanying layer dilation as measured by layer expansion (black) and influx of pore fluid (gray). Equivalent dilation is measured by dividing the volume of influxed water by the frictional contact area. Comparison of the two dilation curves shows fidelity of measurements, and synchronicity indicates that dilatancy hardening is negligible. (b) Raw layer thickness data for the same segment shown in Figure 5a. Dashed line shows linear trend that we remove before analyzing dilation and comparing with fluid dilation, as in Figure 5a.

distance, D_C [*Dieterich*, 1979, 1981]. Our measurements confirm this behavior (Figures 4 and 5a). Although many of our experiments show a slight work hardening trend of increasing frictional strength with shear, friction was nearly constant over the 500–700 μm displacement range of any given velocity step. This is not a dilatancy hardening effect, which would be a function of reduced internal pore pressure in the sheared layer.

[17] In addition to frictional behavior, we measure changes in layer thickness directly, via the DCDT mounted external to the pressure vessel, and also using pore volume changes derived from the influxed fluid volume necessary to maintain constant pore pressure. Each of these measurements show that a step increase in loading velocity produces a simultaneous dilation of the gouge layer, which evolves over a finite slip distance. Figure 5a shows a direct comparison between the two types of dilation measurements with the black line representing actual dilation (measured from the DCDT on the horizontal ram outside of the pressure vessel) of the gouge layer and the dark gray line representing the equivalent layer dilation (based on the measured volume of water injected into the layer in order to maintain constant pore fluid pressure). Differences between the two measurements of dilation are discussed more fully below. Our experiments were conducted at constant applied normal stress and constant applied pore pressure (as measured remote from the layer), therefore any change in pore volume due to dilation or compaction caused an equivalent volume of water to be injected into or withdrawn from the layer, respectively. We define "equivalent dilation" as the volume of fluid injected into the layer as a result of the creation of new pore space during dilation, normalized by the contact area of the side forcing blocks, which does not change during shear.

[18] We measured the friction rate parameter (a-b = $\Delta\mu/\Delta\ln V$) in addition to properties of dynamic layer dilation (Figure 5). We measure a-b after net shear displacements of >3 mm and observe generally negative values of a-b although the values are near zero and positive in a few cases (Table 1).

3.1. Mechanical Response

[19] *Segall and Rice* [1995] used laboratory data from *Marone et al.* [1990] to show that the change in porosity resulting from a change in sliding velocity can be described in the context of rate and state friction using equation (5). At steady state the state variable can be described as $\theta = v/D_C$ where v is the sliding velocity *after* the velocity step, allowing equation (5) to be rewritten as

$$\Delta\phi_{ss} = \varepsilon \ln\left(\frac{v}{v_0}\right), \tag{7}$$

which describes the total porosity change resulting from a change in sliding velocity once steady state has been reached. This relationship tells us that fault zone dilation is controlled by both the size of the velocity step as well as by the dilatancy coefficient ε. Porosity is defined as the ratio of void volume (V_v) to the total volume (V_T) of the gouge layer, and therefore the change in porosity of our gouge layer can be described as

$$\Delta\phi = \phi - \phi_0 = \frac{V_v + \Delta V_v}{V_T + \Delta V_T} - \frac{V_v}{V_T}.$$

Given that effective normal stress was constant in our experiments, changes in the solid volume are zero and measured changes in layer thickness are the result of changes in void volume. Thus, we take $\Delta V_v = \Delta V_T$, and changes in porosity are $\Delta\phi \cong \Delta V_v/V_T$. In our experiments the volumes indicated above are given by the product of the frictional contact area of the sample blocks (5.7 cm × 5.4 cm) and the layer thickness (H), which means that changes in gouge layer porosity are

$$\Delta\phi \cong \frac{\Delta H}{H}. \tag{8}$$

Although we focus primarily on layer dilation, and changes in ΔH, it is useful to compute values of porosity for comparison with other studies. Our uncertainties in porosity are primarily associated with the initial value of layer thickness, which we measure to ±50 μm. The values of $\Delta\phi$ are

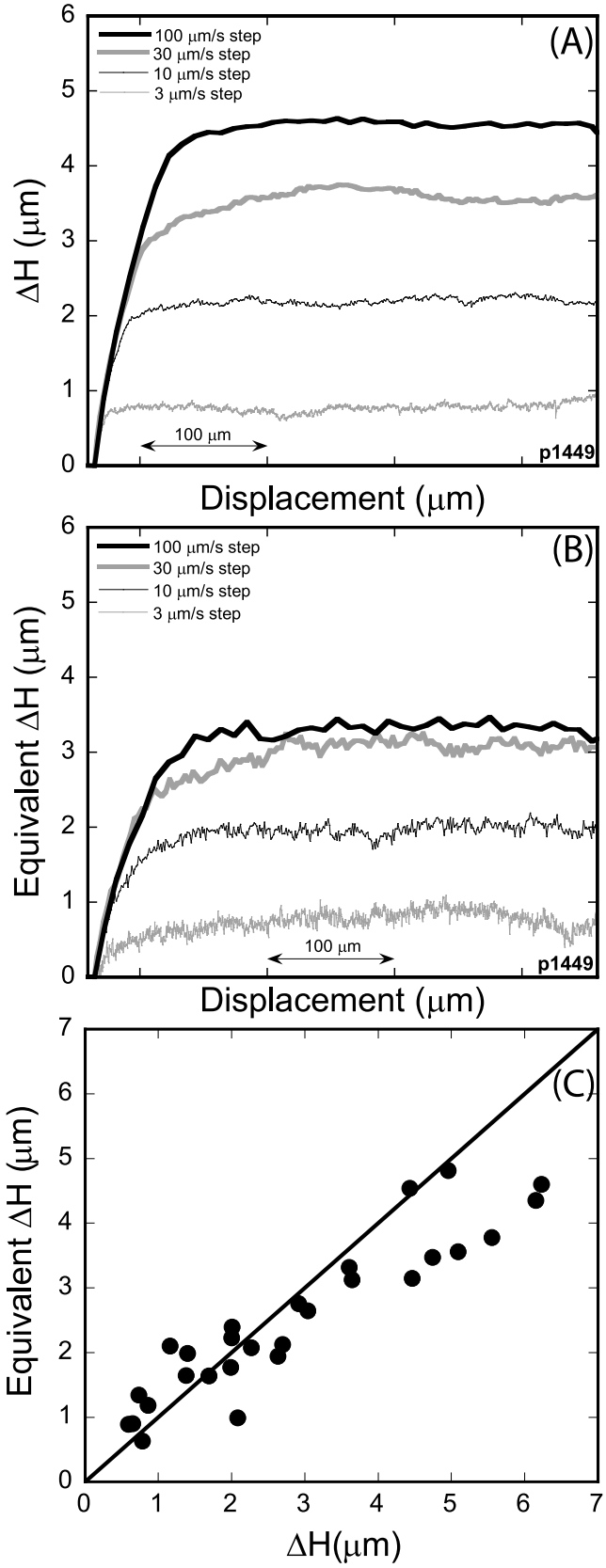

known very precisely because we measure changes in H to ± 0.1 μm.

[20] Gouge layers thin quasi-continuously with slip in direct shear and thus we correct for geometric thinning [e.g., *Scott et al.*, 1994] prior to assessing variations in steady state layer thickness (Figures 4 and 5b). The correction for geometric thinning involves uncertainty associated with the degree to which shear stress has become localized. Thus we remove long-term trends in layer thickness (Figure 5b) before calculating the transient parameter ΔH to determine changes in porosity. When calculating volumetric strain of the layer ($\Delta H/H$) we use a value for layer thickness early in the experiment, after shear displacement has begun, and after any initial dilation when layer thickness was at its maximum (Table 1). We have also calculated ε, using the instantaneous layer thickness, to provide error bars on our measurements of volumetric strain representing the maximum possible interpretation of $\Delta H/H$ based upon our observations.

[21] Equation (7) predicts that the magnitude of fault zone dilation scales with the log of the velocity perturbation. Figure 6 shows a test of this prediction for a set of velocity steps at an effective normal stress of 15 MPa. These data are from a suite of velocity step tests (e.g., Figure 4) and are plotted versus relative shear displacement to allow ready comparison. Of particular note is the similarity of the dilation slip path for each test. Regardless of the size of the velocity step the initial increase in layer thickness with shear slip is nearly identical until the point at which the curve rolls over and a new steady state value of porosity is reached (Figure 6a).

3.2. Fluid Response

[22] Our experiments were run under drained-saturated conditions. As the gouge layer dilated, pore space was created, and pore fluid diffused into the void space as fast as layer permeability allowed. The experimental boundary condition was constant pore fluid pressure (P_P), meaning fluid was injected into the layer if pore fluid pressure within the layer decreased. Measurements of the volume of fluid influx provide an independent constraint on the physical measurements of layer dilation. Figure 6b shows the equivalent dilation of the layer as a function of relative displacement. These data are from the same experiment as Figure 6a and show the strong correlation between the dilation and fluid influx.

Figure 6. (a) Dilation measured by layer expansion versus relative shear displacement for velocity step tests at $\sigma' =$ 15 MPa. Each step starts at 1 μm/s. Darker lines equate to larger velocity steps. Magnitude of dilation increases with increasing velocity step size. Steady state layer thickness is reached in all cases in less than 100 μm displacement. (b) Same as Figure 6a but showing equivalent dilation measured by fluid influx. (c) Equivalent dilation versus physical dilation for all experiments. Physical dilation exceeds fluid dilation at the upper end, for the highest velocity step sizes, which may indicate dilatancy hardening and/or noninterconnected pore space. That these data plot so closely to a 1 to 1 relationship attests to accuracy and precision of the measurements.

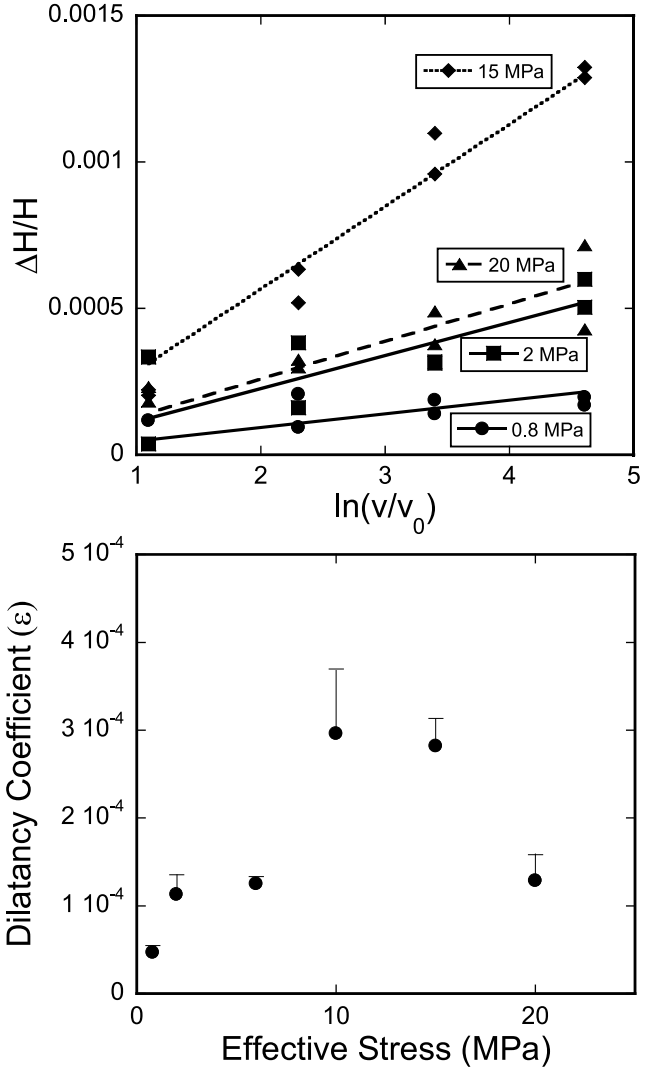

Figure 7. (a) Normalized layer dilation ($\Delta H/H$) versus velocity step size for selected effective normal stresses (0.8, 2, 15, and 20 MPa). $\Delta H/H$ is equivalent to $\Delta\phi$, and thus the slope of each data set defines the dilatancy coefficient, ε. (b) Dilatancy coefficient versus effective normal stress for all experiments. Error bars are calculated by normalizing ΔH by instantaneous layer thickness, rather than steady state thickness, resulting in a maximum possible interpretation of volumetric strain.

3.3. Layer Dilation via Changes in Thickness and Pore Fluid Volume

[23] Comparison of the physical layer dilation with changes in pore volume reveals the extent to which (1) pore pressure remains constant and (2) newly created porosity is interconnected via a fluid pathway. For high permeability gouge, one expects these measurements to show a one to one relationship. Comparison of our data shows a close relationship between dilation and fluid influx (Figure 6c). There is some tendency for misfit at higher velocity steps where the equivalent dilation (Equivalent ΔH) is less than dilation (ΔH) as measured by DCDT. This could indicate that finite permeability of the layer was limiting fluid influx, which would lead to dilatant hardening. However, we attribute discrepancies from the one-to-one line to electrical and experimental noise and possibly to effects associated with geometric thinning of the gouge layer. It is important to note that the maximum differences (Figure 6c) are in the range of 0.05% of the total layer thickness. The similarity of the dilation and equivalent dilation curves (Figures 6a and 6b, respectively) implies that pore volume filled immediately as it was created; otherwise there would be a long-term trend associated with pore fluid slowly filling hydraulically isolated pore space. Another possibility is that porosity is completely isolated hydraulically, but this seems unlikely given that the permeability would have to be several orders of magnitude lower than our measurements.

[24] We can calculate the drainage time for our layers using a characteristic poroelastic diffusion time,

$$t = \frac{H^2\eta(\beta_p + \phi\beta_w)}{2k}, \tag{9}$$

where H is the layer thickness ($\sim$4000 μm), k is the limiting permeability of the system, in this case that of the porous frits ($\sim 4.2 \times 10^{-14}$ m^2), η is the dynamic viscosity of water (0.89×10^{-3} Pa s), β_p is the compressibility of the porous medium ($3.7–6.6 \times 10^{-9}$ Pa^{-1} determined experimentally), ϕ is porosity (we assume 0.2), and β_w is the compressibility of water (4.6×10^{-10} Pa^{-1}). Using these values we calculate a characteristic diffusion time of 6×10^{-4} to 0.001 s, which is sufficiently fast to allow the layer to drain hundreds of times over, even during the 100 μm/s velocity steps which last only 4 s. Ultimately, considering that we are comparing absolute values from independent measurements, using different transducers and calibration techniques, we consider the consistency in dilation seen in Figures 5 and 6 to be remarkable.

3.4. Effective Normal Stress Dependence of ε

[25] The variation in ε with effective normal stress has important implications for earthquake nucleation and rupture physics [*Segall and Rice*, 1995; *Sleep*, 1995, 1997; *Shibazaki*, 2005; *Rice*, 2006]. For granular materials, one might guess that ε would decrease with increasing normal stress as rolling and sliding at lower normal stress give way to fracture and comminution. Our experimental suite was designed to measure the normal stress dependence of ε. Figure 7a shows dilation as a function of $\ln(v/v_0)$, where v_0 is the initial sliding velocity and v is the new sliding velocity for four representative effective normal stresses. Linear best fit lines are shown for each normal stress and the slope is the dilatancy coefficient, ε. Values of ε vary from a minimum of 4.7×10^{-5} at 0.8 MPa to a maximum of 3.0×10^{-4} at 10 MPa. Equation (7) assumes that dilation goes to zero as the velocity step size approaches zero; therefore we forced our linear best fits through zero. We note, however, that some data indicate a nonzero intercept, which could possibly result from a long-term trend of dilation (compaction) and/or picks of ΔH that were not at steady state. Figure 7b shows ε as a function of normal stress for our complete data suite and indicates no clear correlation between ε and σ'. Error bars are derived by normalizing ΔH by the instantaneous layer thickness, rather than the

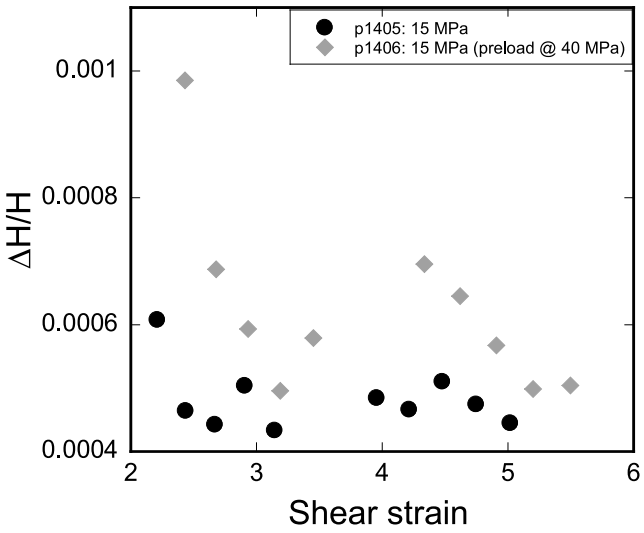

Figure 8. Normalized layer dilation versus shear strain in two experiments conducted at 15 MPa effective normal stress. Experiment p1406 was overcompacted prior to shear (initial effective normal stress of 40 MPa). The loading history and velocity sequence was otherwise identical in both experiments. Note that dilation is initially larger in the overcompacted layer. Dilation values become equal after a shear strain of ~3. Data from p1405 show that dilation reaches a constant value with increasing shear strain.

steady state layer thickness, and show increased scatter in $\Delta H/H$, further indicating the lack of correlation with σ'.

[26] To verify that the relationship between ε and σ' is not an artifact of accumulated strain or the order in which the effective normal stress steps were conducted, we performed sets of tests in which the effective normal stress segments were run in reverse order. These tests were identical to those described above, except that three effective normal stress segments were used. The lowest normal stress segment was run first followed by two higher normal stress segments. These experiments show the same scatter as the data shown in Figure 7, verifying the lack of a clear relationship between ε and effective normal stresses.

3.5. Strain Dependence of ε

[27] In order to investigate the effect of shear strain on dilatancy we conducted tests at a single effective normal stress (15 MPa) and repeatedly varied the sliding velocity from 1 to 10 μm/s over a shear strain of ~5 (18 mm shear displacement). These tests began with the same initial run-in phase used in our normal tests, as described above. Ten velocity steps were conducted over this range of shear strain, and the measured values of $\Delta H/H$ vary only slightly from 0.0006 at a shear strain of 2.2 (8 mm displacement) to 0.00044 at shear strain 5.2 (17.2 mm) (Figure 8). Only the initial velocity step at shear strain 2.2 shows a value of $\Delta H/H$ appreciably larger than 0.0005. Thus, we conclude that over the range of displacements used in our experiments, accumulated strain does not markedly influence the amount of dilation measured in response to a change in sliding velocity.

[28] Although our data do not indicate a systematic variation in ε with effective normal stress, if grain rearrangement at low effective stress gives way to grain comminution at high effective stress, one might expect changes in the value of ε. One possible mechanism for variation of ε with normal stress is through porosity. That is, an overcompacted layer would be expected to dilate more strongly than a normally compacted layer, which would result in larger ε. To the extent that porosity varies inversely with normal stress, [e.g., *Zhang and Cox*, 2000] one would expect that ε would increase with increasing normal stress. To test the hypothesis that increased initial compaction state could lead to increases in ε, we conducted experiments identical to those used to measure strain dependence, except that we first overcompacted the layer by subjecting it to an effective normal stress of 40 MPa for approximately 15 min. Prior to shear, the normal stress was reduced to 15 MPa. Figure 8 shows the raw $\Delta H/H$ measurements of an overcompacted layer (p1406) as a function of strain together with those for a normal experiment (p1405). Note that the velocity step tests for each experiment were conducted at identical shear displacements, but plot at different shear strains due to increased compaction of the layer in p1406. For low shear strains, overconsolidation resulted in significantly larger dilation compared to our conventionally loaded samples (Figure 8). However, as shear strain approached ~3 the normal and overconsolidated layers were similar, within the scatter in the data. These tests indicate that shear-induced dilation decreases with increasing initial porosity, which is consistent with previous work from simple shear tests [e.g., *Terzaghi and Peck*, 1948; *Lambe and Whitman*, 1969].

4. Dilatancy and Fluid Infiltration: Modeling

[29] Initial porosity, antecedent shear velocity, and ambient normal stress each influence the magnitude of dilatancy we observe for perturbations in shearing rate under drained conditions. Where the rate of change in porosity is rapid in comparison to the drainage rate, undrained pore pressures will develop. Compaction and dilation are known to drive pore pressure changes in granular media [*Skempton*, 1954], in fractures [*Goodman*, 1974; *Elsworth and Goodman*, 1985], and in porous fractured aggregates [*Elsworth and Bai*, 1992; *Bai and Elsworth*, 2000]. We evaluate anticipated changes in pore pressure in low-permeability sheared layers embedded within a higher permeability host. In this treatment, the loading by the surrounding host is assumed infinitely stiff, enabling limits on dilatant hardening to be established absent consideration of an elastic feedback.

4.1. Analysis: Governing Equations

[30] Consider a layer of thickness, $2a$, where a is small relative to the lateral extent of the layer (Figure 9). The coordinate system is anchored to the center of the layer, with the x_1 axis aligned perpendicular to the layer, and with the x_2 and x_3 axes layer parallel. The layer is sheared in the x_2 direction at velocities $+v_2/2$ at top ($x_1 = +a$) and $-v_2/2$ at base ($x_1 = -a$), corresponding to a net shear velocity of v_2. We assume that relative velocity is distributed linearly across the layer between these bounding conditions. The layer has an initial porosity of ϕ_0, evolving porosity $\phi(t)$, and directional permeability $k_i(t)$, each of which may evolve over time: we note these as simply ϕ and k in the following,

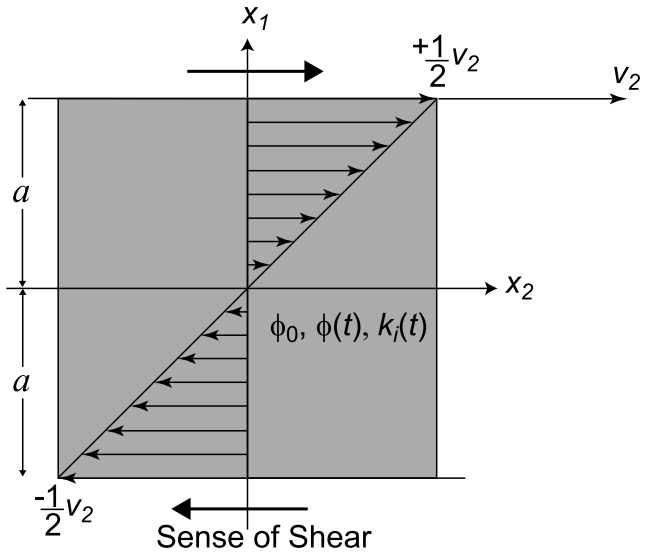

Figure 9. Schematic representation of modeled gouge layer. Shear direction is right lateral and is distributed evenly throughout the layer. Variables are porosity (ϕ), permeability (k), layer half thickness (a), and sliding velocity (v_2).

representing uniform properties. The porous aggregate is saturated by a fluid of modulus, K, density, ρ, and dynamic viscosity, η.

[31] Conservation of the mass rate of flow within the system is defined as [*Bird et al.*, 1960; *Rice and Cleary*, 1976; *Segall and Rice*, 1995; *Segall and Rice*, 2006; *Rice*, 2006]

$$\frac{D\rho}{Dt} + \rho\frac{\partial v_i^f}{\partial x_i} = 0, \tag{10}$$

where the material derivative is defined as

$$\frac{D\rho}{Dt} = \frac{\partial\rho}{\partial t} + v_i\frac{\partial\rho}{\partial x_i},$$

and t is time. Equation (10) may be recast in terms of mass of fluid, m_f, within the pore volume, V_f, as $m_f = V_f\rho$, by substituting into the material derivative to yield

$$\frac{D\rho}{Dt} = \frac{1}{V_f}\frac{Dm_f}{Dt},$$

and on substitution into equation (10) yields

$$\frac{1}{V_f}\frac{\partial m_f}{\partial t} + \frac{1}{V_f}\frac{\partial m_f}{\partial x_i} + \rho\frac{\partial v_i^f}{\partial x_i} = 0. \tag{11}$$

For the one-dimensional (x_1 direction) geometry of interest, the gradient of fluid mass in the x_2 and x_3 directions is null, and the velocity of the solid mass in the x_1 direction is small. Thus the second term of equation (11) disappears. The remaining relation may be recast in terms of fluid pressures by defining appropriate constitutive relations linking fluid pressures with flow velocities and changes in mass due to drainage from the aggregate, or changes in density due to compression of the pore fluid. The rate of transport of the fluid relative to the soil mass is defined through Darcy's law as

$$v_i^f = -\frac{k_i}{\mu}\frac{\partial p}{\partial x_i}, \tag{12}$$

where flow is driven by the excess fluid pressure, p, and moderated by the directional permeability of the granular material, k_i. The rate of fluid mass expelled by the summed effects of compaction of the porous aggregate and compressibility of the fluid is evaluated as

$$\frac{1}{V_f}\frac{\partial m_f}{\partial t} = \frac{\partial\rho}{\partial t} + \frac{\rho}{V_f}\frac{\partial V_f}{\partial t}. \tag{13}$$

The first term represents undrained loading of the aggregate, and may be defined in terms of the compressibility of the fluid as

$$\frac{\partial\rho}{\partial t} = \frac{\partial\rho}{\partial p}\frac{\partial p}{\partial t} = \frac{\rho}{K}\frac{\partial p}{\partial t}.$$

The second term represents the drained compaction of the aggregate, and may be defined in terms of porosity as

$$\frac{\partial V_f}{\partial t} = V\frac{\partial\phi}{\partial t}.$$

Substituting into equation (13) yields

$$\frac{1}{V_f}\frac{\partial m_f}{\partial t} = \frac{\rho}{K}\frac{\partial p}{\partial t} + \frac{\rho}{\phi_0}\frac{\partial\phi}{\partial t}. \tag{14}$$

This evolution function, together with equation (12) may be resubstituted into equation (11), to yield for the single coordinate direction of interest, $x_1 \rightarrow x$,

$$\frac{1}{K}\frac{\partial p}{\partial t} + \frac{1}{\phi_0}\frac{\partial\phi}{\partial t} - \frac{\partial}{\partial x}\frac{k}{\eta}\frac{\partial p}{\partial x} = 0, \tag{15}$$

representing a single expression defined in terms of fluid pressure, p, and the porosity evolution function $\partial\phi/\partial t$, which may be defined from rate and state friction parameters, where once again K and η are the modulus and dynamic viscosity of the pore fluid respectively, and k is the permeability of the layer perpendicular to shear.

4.2. Rate and State Evolution Equations

[32] Porosity evolves from a steady state magnitude, ϕ_0, reached at velocity, v_0, to an evolving new magnitude, ϕ, at shear velocity, v, according to equation (5) [*Segall and Rice*, 1995], $\phi - \phi_0 = -\varepsilon\ln(v_0\theta/D_c)$. When the velocity step first occurs, at $t = 0^+$, the change in porosity is null, and the initial condition for θ is $\theta_0 = D_c/v_0$ which follows directly from equation (5). The evolution parameter may be represented as

$$\frac{d\theta}{dt} = 1 - \frac{\theta v}{D_C}, \tag{16}$$

and this may in turn be used to follow the evolution in porosity as

$$\frac{d\phi}{dt} = \frac{d\phi}{d\theta}\frac{d\theta}{dt}. \tag{17}$$

The individual components of this expression may be compiled by substituting equations (7) and (16), as

$$\left.\begin{aligned}\frac{d\phi}{d\theta} &= \frac{d}{d\theta}\left[\phi_0 - \varepsilon \ln\left(\frac{v_0\theta}{D_c}\right)\right] = -\frac{\varepsilon}{\theta}\\ \frac{d\theta}{dt} &= 1 - \frac{v\theta}{D_c}\end{aligned}\right\} \frac{d\phi}{dt} = -\frac{\varepsilon}{\theta}\left(1 - \frac{v\theta}{D_c}\right). \tag{18}$$

to yield the evolution in porosity with time, as a function of the evolving state parameter, θ. Integrating the evolution law of equation (16), and substituting the initial parameter $\theta_0 = D_c/v_0$ at $t = 0^+$ results in the time evolution of the state parameter as

$$\theta = \frac{D_C}{v}\left[1 + \left(\frac{v}{v_0} - 1\right)e^{-vt/D_C}\right]. \tag{19}$$

The magnitude of θ may be substituted into equation (2) to define the incremental porosity as

$$\phi - \phi_0 = -\varepsilon \ln\left(\frac{v_0\theta}{D_C}\right) = -\varepsilon \ln\left(\frac{v_0}{v}\left[1 + \left(\frac{v}{v_0} - 1\right)e^{-vt/D_C}\right]\right), \tag{20}$$

its evolution in time as

$$\frac{d\phi}{dt} = -\frac{\varepsilon}{\theta}\left(1 - \frac{v\theta}{D_C}\right) = -\varepsilon\frac{v}{D_C}\left(\frac{\left(\frac{v}{v_0} - 1\right)e^{-vt/D_C}}{1 + \left(\frac{v}{v_0} - 1\right)e^{-vt/D_C}}\right), \tag{21}$$

and its ultimate steady state magnitude, ϕ_∞, as

$$\phi_\infty - \phi_0 = -\varepsilon \ln\left(\frac{v_0}{v}\right). \tag{22}$$

Where the fluid is unable to escape from the control volume (undrained loading), then the evolution of pore fluid pressure is defined by

$$\frac{dp}{dt} = -\frac{K}{\phi_0}\frac{d\phi}{dt} \tag{23}$$

or from equation (21),

$$p - p_0 = -\frac{K}{\phi_0}(\phi - \phi_0) = \varepsilon\frac{K}{\phi_0}\ln\left(\frac{v_0}{v}\left[1 + \left(\frac{v}{v_0} - 1\right)e^{-vt/D_C}\right]\right), \tag{24}$$

enabling pore pressure to be evaluated with either the instantaneous porosity, ϕ, or the current time, t. Alternately, the porosity evolution function may be utilized in the governing equation (15) with appropriate boundary conditions to determine the evolution of the pore pressures in the layer, when drainage occurs concurrently with shear augmentation of pore fluid pressures.

4.3. Nondimensional Equations

[33] The behavior of the one-dimensional system is described fully by equation (15) together with the time evolution of the transfer function, $d\phi/dt$, of equation (21), subject to appropriate initial and boundary conditions. It is convenient to represent the combination of equation (21) substituted into equation (15) in dimensionless form. This may be represented as

$$\frac{\partial P_D}{\partial t_D} - \frac{\partial^2 P_D}{\partial x_D^2} - f_D = 0, \tag{25}$$

where for the specific conditions of the Dietrich evolution law,

$$f_D = \frac{1}{\ln\left(\frac{v_0}{v}\right)}V_D\left(\frac{-\left(\frac{v}{v_0} - 1\right)e^{-V_D t_D}}{1 + \left(\frac{v}{v_0} - 1\right)e^{-V_D t_D}}\right). \tag{26}$$

The resulting set of nondimensional parameters is defined as

$$P_D = \frac{\phi}{(\phi_\infty - \phi_0)}\frac{(p - p_0)}{K} = \frac{\phi_0}{\varepsilon \ln\left(\frac{v_0}{v}\right)}\frac{(p - p_0)}{K}, \tag{27}$$

$$t_D = \frac{ct}{a^2}, \tag{28}$$

$$x_D = \frac{x}{a}, \tag{29}$$

$$V_D = \frac{va^2}{cD_C}, \tag{30}$$

defining nondimensional pressure, time, location, and shearing velocity in terms of dimensional parameters of hydraulic diffusivity, $c = (k/\eta)K$, layer half width, a, fluid viscosity, η and final porosity, ϕ_∞. V_D can be restated in terms of two individually dimensionless components as

$$V_D = \frac{a^2}{k}\cdot\frac{v\eta}{KD_C}, \tag{31}$$

where the first term indexes reciprocal drainage rate and the second term the rate of undrained pore pressure generation. Where V_D is small, drainage dissipates undrained pore fluid pressures as rapidly as they form, and the fault response is drained; the converse is true where V_D is large. As will be shown later, the threshold magnitude for a switch from drained to undrained response is for $V_D \sim 1$. Nondimensional pressure is the ratio of the dimensional pore fluid pressure to peak undrained pressure as $t \rightarrow \infty$ (ratio: p/equation (24)), and is bounded as $0 \leq P_D \leq 1$ representing the spectrum of fully drained and undrained responses for a system initially at pressure, p_0. This suite of parameters enables the partially drained pore pressure response to be uniquely defined in terms of

$$P_D = \Im[V_D,\ t_D,\ x_D,\ v/v_0], \tag{32}$$

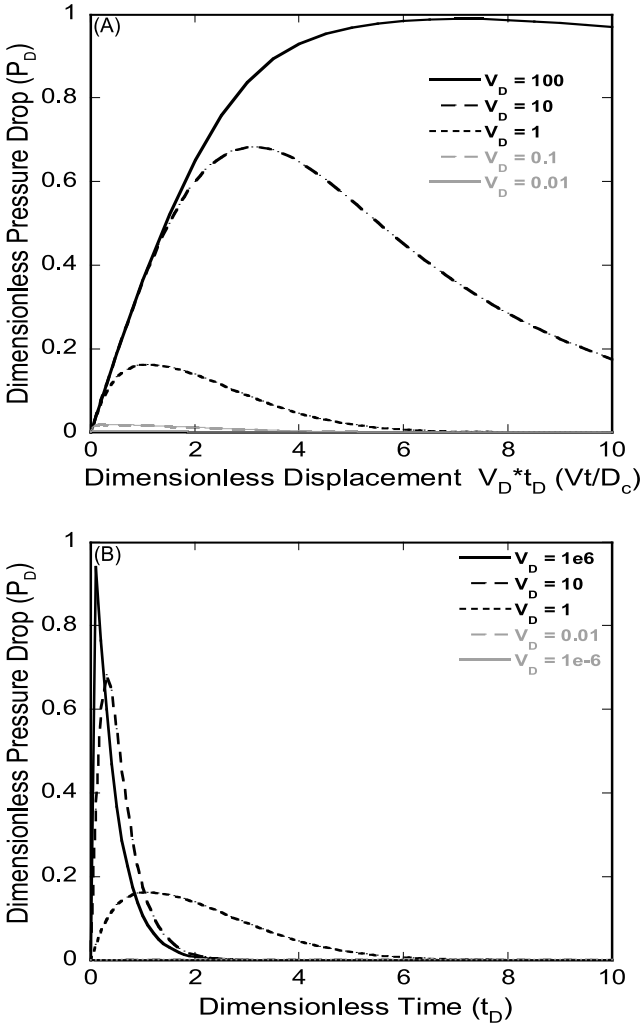

Figure 10. (a) The evolution of dimensionless pressure drop (P_D) is plotted as a function of dimensionless displacement ($V_D t_D$) for varying values of the drainage state (V_D). For the cases shown, a value of V_D = 1 appears to act as a transition between drained and undrained behavior. (b) Evolution of dimensionless pressure drop plotted as a function of dimensionless time (t_D). Again shows that $V_D = 1$ appears transitional between drained/undrained behavior. This is useful in showing the decay of the pore pressure fluctuation back to steady values over time. V_D = 0.01 and 1×10^{-6} lines plot on the x axis.

and the undrained response is defined in terms of a subset of parameters defining pore pressure response in terms of the two parameter groups as $P_D = \Im[V_D t_D, v/v_0]$, or equivalently $P_D = \Im[vt/D_c, v/v_0]$. Where drainage is suppressed, the evolution of dimensionless pressure is given by substituting equations (22) and (24) into equation (27) to give

$$P_D = \ln\left(\frac{v_0}{v}\left[1 + \left(\frac{v}{v_0} - 1\right)e^{-V_D t_D}\right]\right) / \ln\left(\frac{v_0}{v}\right). \qquad (33)$$

Notably, the dilatancy coefficient, ε, is implicitly included within the nondimensional pressure, P_D.

4.4. Parametric Response

[34] For a layer of thickness $2a$, sheared uniformly by bounding velocities $+v_2/2$ at top ($x_1 = +a$) and $-v_2/2$ at the base ($x_1 = -a$), the undrained pore pressure response is determined by equation (33). Where the system is allowed to drain by permeable layer boundaries at $x = \pm a$, the appropriate initial and boundary conditions are defined in terms of nondimensional pressure, $P_D(x_D, t_D)$, as

$$\begin{aligned} &P_D(x_D, t_D < 0) = 0, \\ &P_D(1, t_D \geq 0) = 0, \\ &\frac{\partial}{\partial x_D} P_D(0, t_D \geq 0) = 0, \end{aligned} \qquad (34)$$

and allow the pore fluid pressure response to be followed. For drained boundaries the peak pore pressure is always in the center, at $x_D = 0$, and its evolution may be followed in terms of nondimensional displacement, $V_D t_D$, (Figure 10a), or in terms of nondimensional time, t_D (Figure 10b). The former is useful in observing the build-up of pore pressure in the layer, and the latter for the dissipation response. Apparent from these results is the importance of the parameter $V_D = va2/cD_C$ as a drainage state term in marking the transition between drained and undrained loading.

5. Discussion

[35] Our experiments show that dilation of a granular gouge layer sheared under saturated, drained conditions is nearly synchronous with influx of pore fluid. There is little if any dilatant hardening in our experiments; pore space is filled with water as quickly as it is created. For a less permeable material, with a drainage state term, $V_D \geq 1$ the layer should behave in a quasi-undrained fashion and exhibit dilatant frictional hardening. This type of transient, dilatancy hardening has no effect on steady state frictional behavior, but it would delay the full effectiveness of velocity weakening (strengthening) if the time scale of fluid diffusion and associated strengthening were long compared to the evolution of frictional strength. Transient dilatant hardening would increase the effective value of the friction evolution distance, D_C. Therefore, regardless of its effect on friction velocity dependence, the effect of dilatancy hardening would tend to inhibit the nucleation of seismic slip.

[36] We show that the dilatancy parameter ε is independent of effective normal stress under these experimental conditions. Experiments conducted by *Teufel* [1981] show increasing dilatancy with increases in normal stress, but largely cite crack propagation as the source of dilatancy whereas we suspect grain rearrangement and grain fracture in our experiments. If our results can be applied to seismogenic faults, we would conclude that dilation would be largely independent of depth in a fault zone. We found that ε varies inversely with initial porosity of granular gouge and that the effect weakens with accumulated shear strain. This is consistent with the behavior of overcompacted soils [*Lambe and Whitman*, 1969].

[37] Previous work has documented porosity reduction during the hold portion of slide-hold-slide tests, which are analogous to interseismic periods [*Beeler and Tullis*, 1997; *Karner and Marone*, 2001]. These authors showed that gouge compaction increases linearly with the log of waiting

time. If a similar process occurs in natural fault zones [cf. *Sleep and Blanpied*, 1992], our data indicates that ε and slip-induced dilatancy should increase as a function of increasing earthquake recurrence interval.

[38] The mathematical model we employ assumes that shear, and dilation, are distributed evenly across the gouge layer; it does not intrinsically account for shear localization, though it is inherently accurate over a known shear zone thickness and dilation magnitude. Localization, which may limit the fault zone thickness principally associated with slip to as little as several hundred microns [*Chester and Chester*, 1998; *Chester et al.*, 2003; *Chester and Goldsby*, 2003; *Rice*, 2006], would increase the likelihood and magnitude of fluid depressurization by maximizing the magnitude of the volumetric strain locally, leading to increased effectiveness of shear-induced dilatancy hardening, assuming that the fault zone itself was isolated by way of a low permeability surrounding material.

[39] Calculating a value for V_D using reasonable estimates for the constitutive parameters (K = 2.2 GPa, $\eta = 0.89 \times 10^{-3}$ Pa s, $k = 1 \times 10^{-21}$ m^2, $D_C = 25$ μm) and measurable quantities ($a = 200$ μm, $v = 10$ μm/s, $v_0 = 1$ μm/s, $\phi = 0.15$) yields a value of $\sim$6.5. This conservatively suggests that pore fluid in natural fault zones could be depressurized by as much as 50% leading to significant strengthening. Using more realistic values of v approaching 1 m/s would only serve to increase V_D, indicating stronger fluid depressurization and more effective inhibition of unstable slip via dilatant hardening.

[40] The drainage state term, V_D, expresses a very important control on the magnitude of pore fluid depressurization resulting from dilation, and therefore an important question is: what factors will control V_D in natural fault zones? Spatial variation in V_D presumably would have the effect of limiting the locations where unstable slip could nucleate as well as potentially limiting the areas through which dynamic slip could propagate in a manner similar to that expected for a velocity strengthening frictional rheology. Much like the way a seismic rupture is decelerated, and ultimately arrested, upon propagation into a region of velocity strengthening frictional behavior, one could expect deceleration of ruptures that propagate into regions of saturated fault gouge with high V_D, due to dilational decompression of pore fluids.

[41] The drainage state of a fault zone depends on several terms that can reasonably be expected to vary with depth or along the lateral extent of the fault; fault zone thickness/composition, pore fluid compressibility/viscosity, and perhaps most importantly fault zone permeability. The importance of the thickness of the fault zone in controlling V_D is especially evident because thickness is squared; however it seems unlikely that the principal slip surface of an earthquake varies in thickness over more than 1 or 2 orders of magnitude [*Muir Wood*, 2002; *Tordesillas et al.*, 2004; *Rice*, 2006]. Similarly, neither the bulk modulus nor the viscosity of pore water are likely to change by more than an order of magnitude over the seismogenic depth range [*Bett and Cappi*, 1965; *Franzini and Finnemore*, 1997] without invoking significant changes in water chemistry from gas content or dissolved solids. While perhaps not specifically related to the drainage term, V_D, the fault zone composition could significantly affect the magnitude of fault zone decompression. For instance in a fault zone very rich in clay particles, the associated increase in initial porosity would limit the magnitude of dilational hardening by reducing the volumetric strain associated with any given amount of dilation. Permeability of fault gouge however has been shown to decrease by as many as 7 orders of magnitude over a normal stress range of $\sim$25–200 MPa [*Wibberley*, 2002]. Therefore as depth and stress on any given fault increase it seems likely that changes in permeability are the dominant factor determining V_D. An assumption of our model is that the damage zone surrounding the fault core is sufficiently permeable in comparison to the fault core to supply all fluid necessary to repressurize the fault core as it dilates. *Wibberley and Shimamoto* [2003] suggest that the area immediately surrounding the fault core may be as much as 4 orders of magnitude more permeable than the central slip zone. If, however, the damage zone is also of low permeability this would serve to exacerbate the predictions of our model.

6. Conclusions

[42] We describe a new true triaxial pressure vessel with capabilities for fluid flow during detailed measurements of frictional shearing. Results of our study include two independent measurements of fault zone dilation and the dilatancy coefficient $\varepsilon = \Delta\phi/\Delta\ln(v)$, obtained from velocity stepping tests. We report values of ε for granular quartz subject to shearing rates from 1 to 100 μm/s and effective normal stresses from 0.8 to 20 MPa. We show that the dilatancy coefficient appears to be independent of effective normal stress with a minimum ε of 4.7×10^{-5} at 0.8 MPa and a maximum of 3.0×10^{-4} at 10 MPa. Our results further indicate that reduced initial porosity leads to increased volumetric strain, suggesting increased importance of fault zone dilatancy after long periods of seismic quiescence. We also find that accumulating strain has little effect on the magnitude of ε. Changes in porosity for repeated velocity steps from 1 to 10 μm/s vary from 0.0006 to 0.00044 over 10 mm of slip.

[43] Our experiments show a nearly synchronous creation and infilling of void space indicating the presence of little if any dilatancy hardening. The material tested has very high permeability, on the order of 10^{-13} m^2, indicating that pore fluid can easily diffuse into the layer from the boundaries filling up void space as quickly as it is created by dilation.

[44] Predictions of dilation-induced depressurization in fault gouge based on factors including magnitude of velocity increase, thickness of the gouge layer, and layer perpendicular permeability are obtained. Under reasonable conditions expected for seismogenic depths, shear-induced dilatancy is of sufficient magnitude to completely depressurize pore fluid, thereby inhibiting seismic rupture nucleation or propagation. Our results suggest the need for other, concurrent phenomenon, such as thermal pressurization of pore fluid, or high fault parallel permeability, in order to destabilize creep and nucleate earthquakes within fluid filled fault zones.

Appendix A: True Triaxial Deformation Apparatus

[45] We present here a more detailed description of a novel true triaxial pressure vessel (Figure A1) that extends

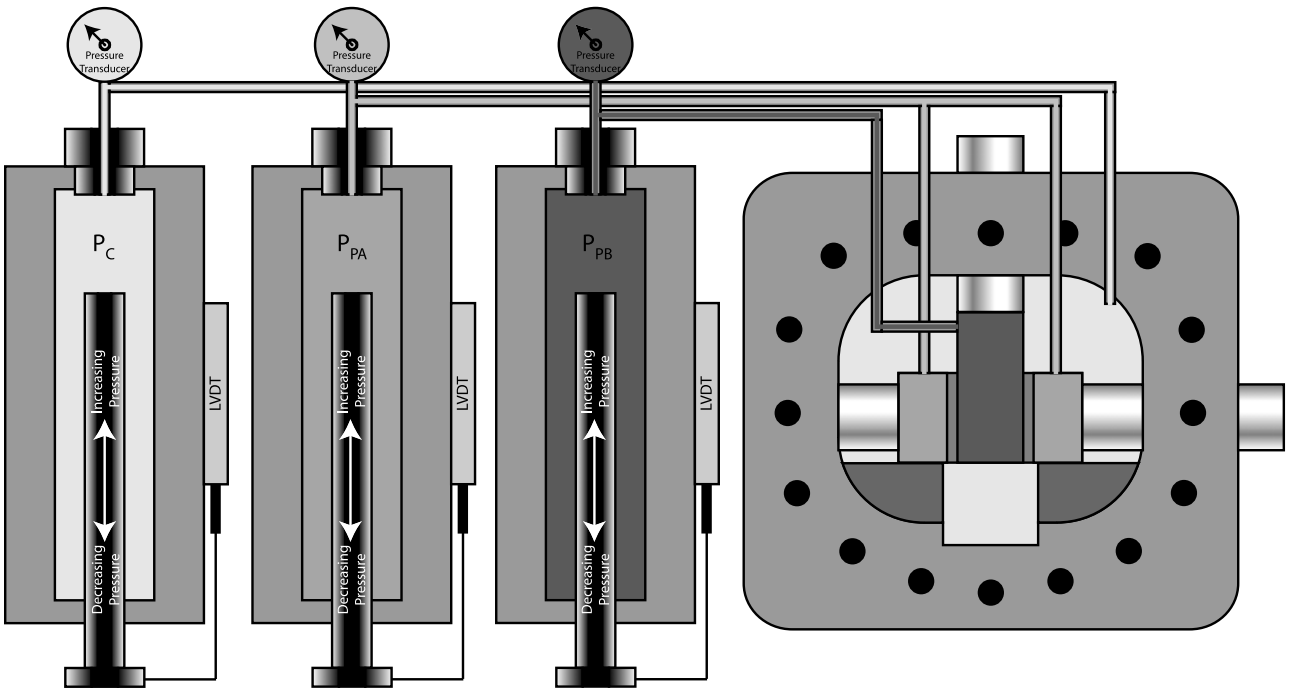

Figure A1. Fluid pressures are supplied to the triaxial pressure vessel through three independently operated pressure intensifiers. One intensifier controls confining pressure P_C using a heat transfer oil. Pore fluid pressures (P_{PA} and P_{PB}) are applied with de-ionized, water. The P_C intensifier is plumbed directly to the vessel, while P_{PA} and P_{PB} are plumbed through the vessel walls and into the forcing blocks via flexible tubing within the pressure vessel.

the capabilities of the biaxial apparatus commonly used for friction measurements in our laboratory (Figure 2). The apparatus shares key features of other true triaxial configurations [e.g., *Haimson and Chang*, 2000], but rather than applying all three stresses via pistons in contact with a prismatic sample, we apply two stresses via loading platens and the third with a fluid confining medium (Figure 2). All three applied stresses are servo controlled and can be set to arbitrary, independent values; with the constraint that applied stresses must be higher than the fluid pressure. In some configurations, including the double-direct shear arrangement used in our experiments, the fluid confining pressure has an effect on normal stress across the layer; however the value of effective normal stress is primarily controlled by the force applied through a piston, and can be set to any arbitrary value. Our testing apparatus is capable of more general stress states than conventional true triaxial machines because we can apply three independent stresses to samples of arbitrary geometry and because we can independently control two pore fluid pressures with flow through the sample during deformation (Figure A1). Easy, direct access to the sample assembly via the removable doors at the front and back (Figure 2) allows a variety of testing modes and sample shapes.

[46] The pressure vessel is capable of maintaining three independent fluid pressures in addition to applied normal and shear stresses on the fault zones (Figure A1). Confining and pore fluid pressures can reach a maximum of 70 MPa. The vertical and horizontal axes of the biaxial load frame apply stresses to the samples via pistons, which access the pressure vessel via sliding, dynamic seals. The loading pistons are precision-milled 44 mm diameter cylinders made of stainless steel. Three separate pressure intensifiers are available to maintain fluid pressures: these are the confining pressure applied to the sample (P_C), and two pore fluid pressures, hereafter referred to as P_{PA} and P_{PB} (Figures A1 and 3). The P_{PA} and P_{PB} fluid pressure intensifiers can be used independently to maintain constant pore pressure boundary conditions or in concert, with a pressure differential, to induce flow in the layer perpendicular to the shear direction using the forcing blocks shown in Figure 3, or parallel to the shear direction using a separate set of forcing blocks. Layer permeability can be measured in situ as a function of shear and normal deformation. Pressure intensifiers are servo controlled and operate by displacing a piston 2.54 cm in diameter within a cylinder with ~25 cm of stroke, which corresponds to a fluid volume of 1.27×10^{-4} m^3. Movement of the piston, measured with linear variable differential transformers (LVDTs), can be controlled in either load- or displacement-feedback servo control to induce either a constant pore pressure or a constant flow rate. All experiments conducted in this study used only one pore pressure intensifier running in load feedback mode to maintain a constant pore pressure. Fluid pressures are monitored by Stellar Technology pressure transducers with greater than 0.007 MPa resolution and can also be monitored manually by analog pressure gauges. Intensifiers were connected to the pressure vessel by 10,000 psi flexible hose manufactured by the Parker Corporation, and fed through the vessel walls via high pressure fluid ports. The confining medium used in these experiments was food grade (nontoxic), paraffinic heat transfer oil (XCELTHERM 600, Radco Industries). Pore

fluid was de-ionized water in the present experiments, though salt water brine has been used in other experiments.

[47] Fluid access to the sample assembly within the pressure vessel is via steel, flexible tubing and high pressure fittings in the sample forcing blocks (Figure 3a). Each forcing block of the double-direct shear arrangement provides fluid access to the layers. Outlet ports in the forcing blocks are surrounded by channels cut into the face of the blocks to evenly distribute fluid. These channels are cut into a recess that accepts porous, sintered stainless steel frits (Mott Corporation) to provide even fluid distribution. The frits are custom cut to fit the recesses in the forcing blocks using an electronic discharge machining (EDM) process. The same EDM process was used to groove the frit surfaces in contact with the fault zones, so as to promote coupling at the layer boundary and shearing within the layer rather than at the boundary between the layer and the frit. Triangular grooves were machined perpendicular to the shear direction and are 1 mm in wavelength and 0.8 mm in depth. The flow distribution frits were 0.5 Media Grade (MG) stainless steel. We conducted in situ, calibration measurements of the frit hydraulic properties, after machining, by conducting permeability experiments without gouge layers. Our frits have an effective permeability of $\geq 4.2 \times 10^{-14}$ m^2. The calibrations include effects of tubing and the finite response time of the pressure intensifiers; thus we can consider that fluid pressure at the layer boundary is constant for effective layer permeabilities below about 5×10^{-15} m^2.

[48] **Acknowledgments.** We gratefully acknowledge support from the National Science Foundation under grants EAR-0510182, EAR-0196570, OCE-064833, EAR-0337627, EAR-0345813, and EAR-0510182, and the U.S. Department of Energy under grant DE-AC02-05CH11231. We thank André Niemeijer, Nick Beeler, Stephen Miller, Dan Faulkner, Gregor Hillers, and two anonymous reviewers for valuable suggestions that helped improve the manuscript.

References

Ampuero, J.-P., and A. M. Rubin (2008), Earthquake nucleation on rate and state faults: Aging and slip laws, *J. Geophys. Res.*, *113*, B01302, doi:10.1029/2007JB005082.

Anthony, J. L., and C. Marone (2005), Influence of particle characteristics on granular friction, *J. Geophys. Res.*, *110*, B08409, doi:10.1029/2004JB003399.

Bai, M., and D. Elsworth (2000), *Coupled Processes in Subsurface Deformation, Flow, and Transport*, 336 pp., ASCE Press, Reston, Va.

Beeler, N. M., and T. E. Tullis (1997), The roles of time and displacement in velocity-dependent volumetric strain of fault zones, *J. Geophys. Res.*, *102*, 22,595–22,609, doi:10.1029/97JB01828.

Bett, K. E., and J. B. Cappi (1965), Effect of pressure on viscosity of water, *Nature*, *207*(4997), 620–621, doi:10.1038/207620a0.

Bird, R. B., W. E. Stewart, and E. N. Lightfoot (1960), *Transport Phenomena*, 770 pp., John Wiley, New York.

Bizzarri, A., and M. Cocco (2006a), A thermal pressurization model for the spontaneous dynamic rupture propagation on a three-dimensional fault: 1. Methodological approach, *J. Geophys. Res.*, *111*, B05303, doi:10.1029/2005JB003862.

Bizzarri, A., and M. Cocco (2006b), A thermal pressurization model for the spontaneous dynamic rupture propagation on a three-dimensional fault: 2. Traction evolution and dynamic parameters, *J. Geophys. Res.*, *111*, B05304, doi:10.1029/2005JB003864.

Bolton, M. D. (1986), The strength and dilatancy of sands, *Geotechnique*, *36*(1), 65–78, doi:10.1680/geot.1986.36.1.65.

Brace, W. F., and J. D. Byerlee (1966), Stick-slip as a mechanism for earthquakes, *Science*, *153*, 990–992, doi:10.1126/science.153.3739.990.

Bridgman, P. W. (1936), Shearing phenomena at high pressure of possible importance for geology, *J. Geol.*, *44*(6), 653–669, doi:10.1086/624468.

Chester, F. M., and J. S. Chester (1998), Ultracataclasite structure and friction processes of the Punchbowl fault, San Andreas system, California, *Tectonophysics*, *295*, 199–221, doi:10.1016/S0040-1951(98)00121-8.

Chester, J. S., and D. L. Goldsby (2003), Microscale characterization of natural and experimental slip surfaces relevant to earthquake mechanics, *SCEC Annu. Progr. Rep. 2003*, South Calif. Earthquake Cent., Los Angeles.

Chester, J. S., A. K. Kronenberg, F. M. Chester, and R. N. Guillemette (2003), Characterization of natural slip surfaces relevant to earthquake mechanics, *Eos Trans. AGU*, *84*(46), Fall Meet. Suppl., Abstract S42C-0185.

Dieterich, J. H. (1978), Time-dependent friction and the mechanics of stick slip, *Pure Appl. Geophys.*, *116*, 790–806, doi:10.1007/BF00876539.

Dieterich, J. H. (1979), Modeling of rock friction 1. Experimental results and constitutive equations, *J. Geophys. Res.*, *84*(B5), 2161–2168, doi:10.1029/JB084iB05p02161.

Dieterich, J. H. (1981), Constitutive properties of faults with simulated gouge, in *Mechanical Behavior of Crustal Rocks: The Handin Volume*, *Geophys/Monogr. Ser.*, vol. 24, edited by N. L. Carter et al., pp. 103–120, AGU, Washington, D. C.

Elsworth, D., and M. Bai (1992), Flow-deformation response of dual porosity media, *J. Geotech. Eng.*, *118*(1), 107–124, doi:10.1061/(ASCE)0733-9410(1992)118:1(107).

Elsworth, D., and R. E. Goodman (1985), Hydromechanical characterization of rock fissures of idealized sinusoidal and sawtooth form, paper presented at International Society for Rock Mechanics Conference on Fundamentals of Rock Joints, Sweden, Sept.

Franzini, J. B., and E. J. Finnemore (1997), *Fluid Mechanics with Engineering Applications*, 9th ed., 807 pp., McGraw-Hill, New York.

Frye, K. M., and C. Marone (2002a), The effect of particle dimensionality on granular friction in laboratory shear zones, *Geophys. Res. Lett.*, *29*(19), 1916, doi:10.1029/2002GL015709.

Frye, K. M., and C. Marone (2002b), Effect of humidity on granular friction at room temperature, *J. Geophys. Res.*, *107*(B11), 2309, doi:10.1029/2001JB000654.

Goodman, R. E. (1974), The mechanical properties of joints, paper presented at Third Congress of the International Society for Rock Mechanics, Denver, Colo., 1–7 Sept.

Haimson, B. C., and C. Chang (2000), A New true triaxial cell for testing mechanical properties of rock, and its use to determine rock strength and deformability of Westerly Granite, *Int. J. Rock Mech. Min. Sci.*, *37*, 285–296, doi:10.1016/S1365-1609(99)00106-9.

Hillers, G., and S. A. Miller (2006), Stability regimes of a dilatant, fluid-infiltrated fault plan in a three-dimensional elastic solid, *J. Geophys. Res.*, *111*, B08304, doi:10.1029/2005JB003872.

Hillers, G., and S. A. Miller (2007), Dilatancy controlled spatiotemporal slip evolution of a sealed fault with spatial variations of the pore pressure, *Geophys. J. Int.*, *168*, 431–445, doi:10.1111/j.1365-246X.2006.03167.x.

Hubbert, M. K., and W. W. Rubey (1959), Role of fluid pressure in mechanics of overthrust faulting 1. Mechanics of fluid-filled porous solids and its application to overthrust faulting, *Geol. Soc. Am. Bull.*, *70*(2), 115–166, doi:10.1130/0016-7606(1959)70[115:ROFPIM]2.0.CO;2.

Ikari, M. J., D. M. Saffer, and C. Marone (2007), Effect of hydration state on the frictional properties of montmorillonite-based fault gouge, *J. Geophys. Res.*, *112*, B06423, doi:10.1029/2006JB004748.

Johnson, P. A., H. Savage, M. Knuth, J. Gomberg, and C. Marone (2008), Effects of acoustic waves on stick-slip in granular media and implications for earthquakes, *Nature*, *451*, 57–61, doi:10.1038/nature06440.

Karner, S., and C. Marone (2001), Fractional strengthening in simulated fault gouge: Effect of shear load perturbations, *J. Geophys. Res.*, *106*(B9), 19,319–19,337, doi:10.1029/2001JB000263.

Lambe, T. W., and R. V. Whitman (1969), *Soil Mechanics*, 553 pp., John Wiley, New York.

Lockner, D., and J. Byerlee (1994), Dilatancy in hydraulically isolated faults and the suppression of instability, *Geophys. Res. Lett.*, *21*(22), 2353–2356, doi:10.1029/94GL02366.

Mair, K., and C. Marone (1999), Friction of simulated fault gouge for a wide range of velocities and normal stresses, *J. Geophys. Res.*, *104*(B12), 28,899–28,914, doi:10.1029/1999JB900279.

Mair, K., K. M. Frye, and C. Marone (2002), Influence of grain characteristics on the friction of granular shear zones, *J. Geophys. Res.*, *107*(B10), 2219, doi:10.1029/2001JB000516.

Marone, C., C. Raleigh, and C. Scholz (1990), Frictional behavior and constitutive modeling of simulated fault gouge, *J. Geophys. Res.*, *95*(B5), 7007–7025, doi:10.1029/JB095iB05p07007.

Mitchell, T. M., and D. R. Faulkner (2008), Experimental measurements of permeability evolution during triaxial compression of initially intact crystalline rocks and implications for fluid flow in fault zones, *J. Geophys. Res.*, *113*, B11412, doi:10.1029/2008JB005588.

Moore, P. L., and N. R. Iverson (2002), Slow episodic shear of granular materials regulated by dilatant strengthening, *Geology*, *30*(9), 843–846, doi:10.1130/0091-7613(2002)030<0843:SESOGM>2.0.CO;2.

Morrow, C. A., and J. D. Byerlee (1989), Experimental studies of compaction and dilatancy during frictional sliding on faults containing gouge, *J. Struct. Geol.*, *11*(7), 815–825, doi:10.1016/0191-8141(89)90100-4.

Muir Wood, D. (2002), Some observations of volumetric instabilities in soils, *Int. J. Solids Struct.*, *39*, 3429–3449, doi:10.1016/S0020-7683(02)00166-X.

Niemeijer, A., C. Marone, and D. Elsworth (2008), Healing of simulated fault gouges aided by pressure solution: Results from rock analogue experiments, *J. Geophys. Res.*, *113*, B04204, doi:10.1029/2007JB005376.

Perfettini, H., and J.-P. Ampuero (2008), Dynamics of a velocity strengthening fault region: Implications for slow earthquakes and postseismic slip, *J. Geophys. Res.*, *113*, B09411, doi:10.1029/2007JB005398.

Rathbun, A. P., C. Marone, R. B. Alley, and S. Anandakrishnan (2008), Laboratory study of the frictional rheology of sheared till, *J. Geophys. Res.*, *113*, F02020, doi:10.1029/2007JF000815.

Rice, J. R. (2006), Heating and weakening of faults during earthquake slip, *J. Geophys. Res.*, *111*, B05311, doi:10.1029/2005JB004006.

Rice, J. R., and M. P. Cleary (1976), Some basic stress diffusion solutions for fluid saturated elastic porous media with compressible constituents, *Rev. Geophys. Space Phys.*, *14*(2), 227–241, doi:10.1029/RG014i002p00227.

Rice, J., and J. W. Rudnicki (1979), Earthquake precursory effects due to pore fluid stabilization of a weakening fault zone, *J. Geophys. Res.*, *84*(B5), 2177–2193, doi:10.1029/JB084iB05p02177.

Rubin, A. M. (2008), Episodic slow slip events and rate and state friction, *J. Geophys. Res.*, *113*, B11414, doi:10.1029/2008JB005642.

Rubin, A.M., and J.-P. Ampuero (2005), Earthquake nucleation on (aging) rate and state faults, *J. Geophys. Res.*, *110*, B11312, doi:10.1029/2005JB003686.

Rudnicki, J. W., and C.-H. Chen (1988), Stabilization of rapid frictional slip on a weakening fault by dilatant hardening, *J. Geophys. Res.*, *93*(B5), 4745–4757, doi:10.1029/JB093iB05p04745.

Rudnicki, J. W., and T.-C. Hsu (1988), Pore pressure changes induced by slip on permeable and impermeable faults, *J. Geophys. Res.*, *93*(B4), 3275–3285, doi:10.1029/JB093iB04p03275.

Rudnicki, J. W., and J. Rice (2006), Effective normal stress alteration due to pore pressure changes induced by dynamic propagation on a plane between dissimilar materials, *J. Geophys. Res.*, *111*, B10308, doi:10.1029/2006JB004396.

Ruina, A. (1983), Slip instability and state variable friction laws, *J. Geophys. Res.*, *88*(B12), 10,359–10,370, doi:10.1029/JB088iB12p10359.

Saffer, D. M., and A. W. McKiernan (2005), Permeability of underthrust sediments at the Costa Rican subduction zone: Scale dependence and implications for dewatering, *Geophys. Res. Lett.*, *32*, L02302, doi:10.1029/2004GL021388.

Samuelson, J., C. Marone, B. Voight, and D. Elsworth (2008), Laboratory investigation of the frictional behavior of granular volcanic material, *J. Volcanol. Geotherm. Res.*, *173*, 265–279, doi:10.1016/j.jvolgeores.2008.01.015.

Savage, H. M., and C. Marone (2007), Effects of shear velocity oscillations on stick-slip behavior in laboratory experiments, *J. Geophys. Res.*, *112*, B02301, doi:10.1029/2005JB004238.

Savage, J. C., and J. Langbein (2008), Postearthquake relaxation after the 2004 M6 Parkfield, California, earthquake and rate-and-state friction, *J. Geophys. Res.*, *113*, B10407, doi:10.1029/2008JB005723.

Scholz, C. (1988), Mechanisms of seismic quiescences, *Pure Appl. Geophys.*, *126*(2–4), 701–718, doi:10.1007/BF00879016.

Scholz, C. (2002), *The Mechanics of Earthquakes and Faulting*, 2nd ed., 496 pp., Cambridge Univ. Press, Cambridge, U. K.

Scott, D., C. Marone, and C. Sammis (1994), The apparent friction of granular fault gouge in sheared layers, *J. Geophys. Res.*, *99*(B4), 7231–7246, doi:10.1029/93JB03361.

Segall, P., and J. Rice (1995), Dilatancy, compaction, and slip instability of a fluid-infiltrated fault, *J. Geophys. Res.*, *100*(B11), 22,155–22,171, doi:10.1029/95JB02403.

Segall, P., and J. Rice (2006), Does shear heating of pore fluid contribute to earthquake nucleation?, *J. Geophys. Res.*, *111*, B09316, doi:10.1029/2005JB004129.

Shibazaki, B. (2005), Nucleation process with dilatant hardening on a fluid-infiltrated strike-slip fault model using a rate- and state-dependent friction law, *J. Geophys. Res.*, *110*, B11308, doi:10.1029/2005JB003741.

Skempton, A. W. (1954), The pore pressure coefficients A and B, *Geotechnique*, *4*, 143–147, doi:10.1680/geot.1954.4.4.143.

Sleep, N. H. (1995), Frictional heating and the stability of rate and state dependent frictional sliding, *Geophys. Res. Lett.*, *22*(20), 2785–2788, doi:10.1029/95GL02801.

Sleep, N. H. (1997), Application of a unified rate and state friction theory to the mechanics of fault zones with strain localization, *J. Geophys. Res.*, *102*, 2875–2895, doi:10.1029/96JB03410.

Sleep, N. H., and M. L. Blanpied (1992), Creep, compaction and the weak rheology of major faults, *Nature*, *359*, 687–692, doi:10.1038/359687a0.

Song, I., and J. Renner (2008), Hydromechanical properties of Fontainbleau sandstone: Experimental determination and micromechanical modeling, *J. Geophys. Res.*, *113*, B09211, doi:10.1029/2007JB005055.

Terzaghi, K., and R. B. Peck (1948), *Soil Mechanics in Engineering Practice*, 566 pp., John Wiley, New York.

Teufel, L. W. (1981), Pore Volume Changes During Frictional Sliding of Simulated Faults, in *Mechanical Behavior of Crustal Rocks: The Handin Volume*, *Geophys/Monogr. Ser.*, vol. 24, edited by N. L. Carter et al., pp. 135–145, AGU, Washington, D. C.

Tordesillas, A., J. F. Peters, and B. S. Gardiner (2004), Shear band evolution and accumulated microstructural development in Cosserat media, *Int. J. Numer. Anal. Methods Geomech.*, *28*, 981–1010, doi:10.1002/nag.343.

Wibberley, C. A. J. (2002), Hydraulic diffusivity of fault gouge zones and implications for thermal pressurization during seismic slip, *Earth Planets Space*, *54*, 1153–1171.

Wibberley, C. A. J., and T. Shimamoto (2003), Internal structure and permeability of major strike-slip fault zones: The Median Tectonic Line in Mie Prefecture, southwest Japan, *J. Struct. Geol.*, *25*, 59–78, doi:10.1016/S0191-8141(02)00014-7.

Zhang, S., and S. F. Cox (2000), Enhancement of fluid permeability during shear deformation of a synthetic mud, *J. Struct. Geol.*, *22*, 1385–1393, doi:10.1016/S0191-8141(00)00065-1.

D. Elsworth, C. Marone, and J. Samuelson, Rock and Sediment Mechanics Laboratory, Center for Geomechanics, Geofluids, and Geohazards, and Energy Institute, Pennsylvania State University, 312 Deike Bldg., University Park, PA 16802, USA. (jsamuels@geosc.psu.edu)